Polar methylammonium organic cations detune state coupling and extend hot carrier lifetime in lead halide perovskites

Cheng Wang,^{1#} Weibin Chu,^{2#} Feihong Ye,¹ Zhenwei Ou,¹ Zhe Li,¹ Quanbing Guo,¹

Xiaoze Liu,¹ Guojia Fang,¹ Oleg Prezhdo,² Ti Wang,^{1*} and Hongxing Xu^{1*}

¹ School of Physics and Technology, and Key Laboratory of Artificial Micro- and Nano-structures of Ministry of Education, Wuhan University, Wuhan 430072, China

² Department of Chemistry, and Department of Physics and Astronomy, University of Southern California, Los Angeles, CA 90007, USA

[#] These authors contributed equally to this work

^{*} Correspondence: wangti@whu.edu.cn

^{*} Correspondence: hxxu@whu.edu.cn

SUMMARY

The slow hot-carrier relaxation properties of lead halide perovskites show great promise for hot carrier solar cells. Here, we discover the hot carrier relaxation could be prolonged by two orders of magnitude in lead halide perovskites. By ultrafast spectroscopy, we unravel a slow hot-carrier relaxation process mediated by an intermediate state above the conduction band minimum (CBM). This intermediate state is formed by incorporating polar methylammonium (MA) cations. The first-principle calculation further confirms that the incorporation of MA cations introduces a prolonged relaxation process from CBM+1 to CBM state, which are the split-off states of CBM due to the strong spin-orbit coupling. The prolonging effect is interpreted that MA cations largely increase the lattice distortions and detune their inter-state coupling. This work reveals a neglected way to prolong the hot carrier relaxation processes and provides guidance for the hot carrier photovoltaics to overcome the current Shockley-Queisser limit.

KEYWORDS

Hybrid perovskite, hot carrier, Shockley-Queisser limit, spin-orbit coupling.

INTRODUCTION

The power conversion efficiency (PCE) of a single junction solar cell cannot be improved endless, which is restricted by the Shockley-Queisser (S-Q) limit. In physics, the S-Q limit is the maximum theoretical efficiency which is calculated as a function of the energy bandgap. Even with the optimal band gap of 1.34 eV, the PCE can reach the maximum efficiency around 33%. Since the first report of MAPbI₃ photovoltaics in 2009,² hybrid organic-inorganic lead halide perovskite solar cells (PSCs) have been rapidly developing in the past decade, and approaching the S-O limit with a world record PCE of 25.5% so far. 3-6 The current S-O limit is theoretically calculated by assuming the rapid hot-carrier relaxation of few picoseconds (ps) as the intrinsic energy dissipation. This assumption becomes controversial when ultralong hotcarrier cooling processes mediated by the hot phonon bottleneck effect have been observed in lead halide perovskites (LHP).. $^{7-12}$ This effect slows down the hot-carrier cooling rate ($\sim 10^{-2}$ ps $^{-1}$ 1) by two orders of magnitude, 10,13-17 challenging the calculated S-Q limit. 18 Even though the hot phonon bottleneck effect occurs at high excitation densities which are generally not satisfied in photovoltaic tests, it implies that the S-Q limit could be underestimated if the hot-carrier relaxation is prolonged significantly.

The control of hot-carrier relaxation has then been one of the most critical tasks to improve the photovoltaic performance with LHPs (ABX₃). The inorganic BX₃⁻ framework is primarily responsible for the near-edge states, whereas the A-site cations are thought to only assist the crystal lattice stabilization. ¹⁹⁻²¹ It is later suggested different A-site cations can significantly impact hot carrier cooling processes. ^{10,22} Specifically, the incorporation of alkali A-site cations

can reduce excitation densities for the hot phonon bottleneck,¹² which are still two orders of magnitude higher than the one sun illumination in photovoltaic test conditions. With these efforts, prolonging the hot-carrier relaxation seems a quite difficult issue, but is yet to be resolved. In this context, we discover the hot-carrier relaxation time is prolonged by two orders of magnitude to be one hundred ps, by simply incorporating polar MA cations into FAPbI₃ films.

The prolonging effect results from slow carrier dynamics through an intermediate state above the conduction band minimum (CBM). By ultrafast transient dynamic measurements and theoretical modeling, an ultralong hot-carrier relaxation time of 98 ps from the intermediate state (CBM+1) to the CBM is identified when incorporating MA cations. Combining with first-principle calculation, the intermediate state CBM+1, about 0.72 eV split-off of CBM, 23,24 is attributed to the strong spin-orbit coupling (SOC) involving heavy Pb and I elements. The incorporated MA cations are analyzed to enhance the detuning between CBM+1 and CBM and weaken their inter-state coupling. This prolonging effect is applicable to the low excitation densities and can support a long relaxation time under the standard AM1.5G illumination of photovoltaic tests. This work provides neglected but important guidance for the LHP photovoltaics to overcome the current S-Q limit.

RESULTS AND DISCUSSION

The FAMAPbI₃ thin films were synthesized by a two-step sequential deposition method.²⁶ A thin layer of PbI₂ was firstly deposited on glass substrates. After annealing, the FAI solutions

(60 mg/mL) with different amounts of MACl additives (*x* mg/mL) were spun cast atop the predeposited PbI₂ layer. Further details of the thin film preparation can be found in the Method section. In this work, the *x* value was set to 0, 6, 10, and 14. The corresponding samples are denoted as MACl-*x* (i.e. MACl-0, MACl-6, MACl-10, and MACl-14). Figure 1A schematically shows the crystal structure of hybrid perovskites APbI₃. The A-site can be weak polar FA or strong polar MA cations.

It is noted that the incorporation of MA cations into the FAPbI₃ lattice will lead to the bandgap and lattice change. To confirm the exact MA ratio, X-ray diffraction (XRD) measurements have been performed, and the respective patterns are presented in Figure 1B. To distinctly clarify the effects by incorporating MA cations, the XRD results of MACl-0 and MACl-14 are shown in Figure 1B. The results of MACl-6 and MACl-10 are presented in the supplemental information (Figure S1). The (110) XRD reflection peaks at ~14° and the (220) peak at $\sim 28^{\circ}$ show a typical perovskite α phase, while the peak of the non-perovskite δ phase is absent in all the samples. The diffraction peaks marked with a green star are related to PbI₂. It is noted that the peak position of the (110) plane can be utilized to estimate the actual MA ratio in the thin films.²⁷ As shown in Figure S1, the range near the (110) diffraction peak has been zoomed in and the exact peak positions are extracted as depicted in Figure 1C. With the increase of MACl stoichiometry, the incident angle of the (110) plane shifts to the lower site. According to the Bragg equation, the pseudo-cubic interplanar spacing d_{110} can be calculated from the incident angles, which shows a linear correlation with the MA ratio (Figure. 1C). Therefore, the MA actual ratio of MACl-6, MACl-10, and MACl-14 can be assigned as ~ 0.02, ~ 0.05 , and ~ 0.10 , respectively (supplemental information Table S1). Thus, these results demonstrate that MA cations have been incorporated into the FAPbI₃ lattice inducing the shift of XRD peaks.

Figure 1D shows the ultraviolet-visible (UV-vis) absorption and steady-state photoluminescence (PL) spectra of these perovskite thin films. With the incorporation of MA cations, the absorption edge of MACl-14 has a slight blueshift compared to that of MACl-0. Notably, MAPbI₃ has a larger bandgap compared to FAPbI₃. Thus, the blueshift of the absorption edge further implies that MA cations have been incorporated into the FAPbI₃ crystal lattice. Moreover, the PL spectra also exhibit a blueshift after introducing MA cations which is consistent with the UV-vis results.

To investigate the carrier dynamics simultaneously after photon excitation, transient absorption (TA) spectroscopy has been performed on different samples with identical experimental conditions. Figures 2A and B illustrate typical pseudo color TA plots of MACl-0 and MACl-14 with an excitation photon energy of 3.10 eV. For all samples, a ground state bleaching band centered around the bandgap is observed due to the band-filling effect. Received a photoinduced absorption (PIA, positive signal in $\Delta T/T$) signal below the bandgap is also observed at delay time shorter than 1 ps, which have been assigned to hot carriers. Here, we focus on the dynamics of the bleaching peak which is associated with the density of carrier at the CBM. The bleaching peak positions of MACl-0 and MACl-14 are at 797 and 778 nm, respectively. The slight blueshift is consistent with the PL and absorption results. It is worth noting that the bleaching signal reaches the maximum immediately within the excitation light for MACl-0. However, for MACl-14 samples, a slow-rising component has been observed and

the maximum signal appears almost at the delay time of 200 ps. Figure 2C presents the extracted carrier dynamics at bleaching peak positions. Compared to MACl-0, a slow-rising component can be distinctly distinguished for MACl-14 samples. In addition, previous works have illustrated that the Cl ions have evaporated from the perovskite thin films with the incorporation of MACl additives. Thus, this slow-rising component should not be caused by the effects of Cl ions. The only difference between the MACl-0 and MACl-14 samples is the incorporation of MA cations, which should be the origin for the slow-rising component.

This slow-rising component cannot be explained by a two-level energy system. The detailed analysis can be found in the supplemental information (Notes S1-S3). After excluding the possible mechanisms in a two-level energy system, a three-level energy system model is proposed to depict the slow-rising component (Figure 2D). Here, we propose that an intermediate state (IS) above the CBM results in the slow-rising component. Photogenerated carriers at excited states (ES) can directly cool down to the CBM with a rate of k_2 , or through the IS with a rate of k_1 . The carriers at IS can then relax to the CBM with a slow rate of k_3 . With this model, the slow-rising component is from the carrier relaxation through IS to the CBM. The differential rate equations can be expressed as follow:

$$\frac{\mathrm{d}n}{\mathrm{d}t} = -k_1 n - k_2 n \tag{1}$$

$$\frac{\mathrm{d}n_1}{\mathrm{d}t} = k_1 n - k_3 n_1 \tag{2}$$

$$\frac{\mathrm{d}n_2}{\mathrm{d}t} = k_2 n + k_3 n_1 - k_4 n_2 n_h - k_5 n_2 \tag{3}$$

with the initial condition $n(t=0)=N_0$. Here, n, n_1, n_2 , and n_h refer to electron densities in the ES, IS CBM, and the hole density in the valence band maximum (VBM), respectively; k_1, k_2 , and k_3 are the relaxation rates from ES to IS, ES to CBM, and IS to CBM, respectively; k_4 is the bimolecular charge carrier recombination rate; k_5 is the trap-assisted carrier recombination rate; N_0 is the initial photoexcited carrier density. To simplify the model, three assumptions are made here. First, with a low excitation density, the carrier density almost keeps the maximum in a few nanoseconds after the incorporation of MA cations. Thus, in the first 200 ps, the trap-assisted carrier recombination can be neglected. Second, we assume the perovskite samples are not doped by electrons and holes. Thus, it generates an equal quantity of free electrons and holes in perovskites under the photon excitation (i.e. $n_2 = n_h$). Third, since the excitation density is low enough (N_0 less than $1.2 \times 10^{18} \text{cm}^{-3}$), there are no carrier-carrier annihilation and other high order recombination processes. Thus, Equation (3) can be simplified to:

$$\frac{\mathrm{d}n_2}{\mathrm{d}t} = k_2 n + k_3 n_1 - k_4 n_2^2 \tag{4}$$

The fitting details are given in the supplemental information (Note S4). With this model, the fitting curve matches the data properly (solid line in Figure 2C).

To investigate the origin of the slow-rising component and the properties of the IS, we conduct TA experiments on various samples. Figure 3A shows the bleaching dynamics for samples with different MA ratios. The excitation photon energy is fixed to 3.10 eV and the excitation densities are all the same. It shows that a slow-rising component simultaneously

appears after incorporating MA cations. With a higher MA ratio, the slow-rising component becomes more obvious. The solid lines in Figure 3A are the fitting results by the previous model and the fitting parameters are shown in the supplemental information (Table S2). It presents a slower k_3 with a higher MA ratio. The rate k_3 decrease from 3.3 ×10¹⁰ s⁻¹ for MACl-6 to 1.1 ×10¹⁰ s⁻¹ for MACl-14. In addition, to quantify the portion of carriers relaxing through IS, the parameter N_1/N_0 is calculated from the model (Figure S4), where the N_1 is the maximum value of $n_1(t)$. It shows an opposite trend compared to k_3 . The N_1/N_0 increases from 9.8% for MACl-6 to 30.7% for MACl-14. Thus, it can be speculated that both k_3 and N_1/N_0 change as a function of the MA ratio. The higher MA ratio will increase both the relaxation time from IS to CBM and the portion of carriers relaxing through IS (Figure 3D). With these results, we can further confirm that the slow-rising component originates from the organic MA cation.

To study the physics behind the slow-rising component, we perform systematic TA measurements on the MACl-14 sample. Figure 3B shows a power dependence of TA spectra with the excitation photon energy of 3.10 eV. Here, excitation densities are all controlled in a relatively low region (N_0 less than 1.2 ×10⁻¹⁸ cm⁻³), in which the high order recombination processes can be ignored. Therefore, we can use the model discussed above to simulate all the dynamics curves (the solid lines in Figure 3B), and the fitting parameters are presented in Table S4. Two main conclusions can be reached by the power dependence results. First, the value of N_1/N_0 (Figure 3E) is 32.2±0.6% which does not vary with the increase of excitation densities. This finding is reasonable because the pump power only changes the initial carrier density N_0 , whereas the proportion of carriers relaxing through IS to CBM should be determined by the coupling strength of the states between the IS and CBM. Second, the k_3 rate in Figure 3E is

almost around $1.91 \pm 0.32 \times 10^{10}$ s⁻¹. With the increase of the excitation density, it has a gradually faster relaxation rate, which could be explained by the multiparticle effect at high excitation densities at the IS. Significantly, the slowest k_3 corresponds to a characteristic lifetime of 98 ps, which is two orders of magnitude longer than other hybrid halide perovskites.^{22,33,34}

If this three-level system scenario is correct, one can imagine that the slow-rising component should not be detected once the excitation photon energy is lower than the IS. To demonstrate this scenario and estimate the energy level position of the IS, Figure 3C presents the carrier dynamics under various excitation photon energies. The fitting parameters are presented in Figure 3F and the supplemental information (Table S4). Although the photon energies are different, the excitation powers are set to the same value to exclude the divergence of the excitation photon energy differences. It is noted that the slow-rising component is more distinct with a higher excitation photon energy. Interestingly, the relaxation rate from IS to CBM, i.e. k_3 , almost keeps constant under different photon energies (Figure 3F). Since the k_3 reflects the rate from IS to CBM which is dependent on the coupling strength between IS and CBM, it should be irrelevant to the excitation photon energy under a low excitation density. However, the parameter N_1/N_0 exhibits a lower numerical value with a smaller photon energy. The previous power dependence results have demonstrated that the factor N_1/N_0 is independent of excitation densities (Figure 3E). Thus, this decrease should not be caused by the different excitation photon energies. The portion of N_1/N_0 decreases from 33% with a photon energy of 3.10 eV to only 5% with a photon energy of 2.38 eV. Therefore, we can estimate that the IS is about 2.35 eV above the VBM from this trend. To further confirm the position of the IS, the reflection spectrum of MACl-14 has been performed and the differential reflectivity spectrum is presented in Figure S6. It shows a pronounced peak at 2.35 eV which is consistent with the TA results.³⁵

To gain further insights into the origin of the IS, ab initio simulations have been performed. The SOC is a relativistic interaction that can lead to shifts in energy levels. The errors introduced by electron self-interaction in the PBE functional and neglect of SOC fortunately cancel each other in lead halide perovskites. Thus, the PBE functional has been widely used without consideration of SOC. However, this brings a significant issue that has been surprisingly overlooked for a long period. Besides the dynamic Rashba effect, dramatic spinorbit split-off of the conduction bands exists in perovskites, and it should significantly impact the hot carrier relaxation process. To simulate the experiment condition, FAPbI₃ and FA_{0.875}MA_{0.125}PbI₃ are chosen as the model systems for the calculation. After consideration of the SOC, the spin-orbit split-off between the p-like orbitals of total angular momentum J=3/2 and J=1/2 amount is about 0.72 eV (Figures 4B and D), which is consistent with previous calculations and the IS position in our results.^{23,36} Thus, we attribute the IS in the experimental observation to the CBM+1 state which is the split-off states of CBM due to the SOC. In this scenario, CBM+1 (J=3/2) should behave as an intermediate state, and the excited electrons are expected to stay on this state in both FAPbI₃ and FA_{0.875}MA_{0.125}PbI₃. However, the long-lived hot carriers are only observed if FAPbI₃ is incorporated with MA. To understand this discrepancy, we investigate the behavior of the SOC split-off during hot electron relaxation under ambient conditions. Due to the notoriously expensive cost of the HSE+SOC calculation, we calculate HSE+SOC electronic structures of 15 snapshots which are randomly chosen from

the real-time trajectories. As shown in the red areas of Figures 4E, G and Figure S6, the electronic structures vary greatly in FAPbI₃, while they change much less in FA_{0.875}MA_{0.125}PbI₃ (Figures 4F and H). In particular, the gap between CBM and CBM+1 becomes small more often in FAPbI₃ than FA_{0.875}MA_{0.125}PbI₃. This indicates that electron-phonon coupling is more significant for the hot electron relaxation in FAPbI₃. Although there is a large split-off of CBM and CBM+1 in FAPbI₃ at 0 K, such a strong electron-phonon coupling at room temperature can assist the hot electron relaxation process leading to a faster relaxation from CBM+1 to CBM. Conversely, the state manifold remains sparse and CBM is isolated for all geometries investigated in FA_{0.875}MA_{0.125}PbI₃, which implies a week electron-phonon coupling. Thus, the electrons can remain hot after the incorporation of organic MA cations.

Noteworthy, the only difference in these two systems is the incorporation of MA cations. The weakened electron-phonon coupling in FA_{0.875}MA_{0.125}PbI₃ can be rationalized with the strong anharmonicity which is impacted by the MA cation. Not only the organic A-site cation assists the lattice stabilization, but also it plays an essential role in the electronic and dynamic properties of lead halide perovskites. For instance, polar organic A-site cations are prone to form hydrogen bonds with the inorganic metal-halide sublattice, which can alter the covalent/ionic character of the metal-halide bonds. Moreover, the local polar fluctuation induced by the A-site cation head-to-head displacement coupling to the octahedral distortion is responsible for the strong anharmonicity and dynamic disorder.³⁷ Note that the MA cation is more polar than the FA cation, leading to stronger lattice distortions. Such dynamic disorder can localize charge distribution and decouple the carriers in the CBM+1 and CBM states.

molecular dynamics to investigate whether the MA cation incorporation enhances the dynamic disorder that can be responsible for the observed outstanding long lifetime of carriers in the IS. Compared to the conventional semiconductor TiO₂ (Figure. 4I), the mean square displacement (MSD) of the inorganic lattice along the 10 ps trajectory (Figure. 4J) demonstrates that both the FAPbI₃ and FA_{0.875}MA_{0.125}PbI₃ systems exhibit an order of magnitude larger fluctuations than TiO₂. Notably, the MA incorporation enhances the dynamic disorder further, which can be rationalized by the strong dipole of MA cations. Thus, the incorporation of polar MA cations detunes the coupling between the CBM+1 and CBM states, resulting in a long lifetime of charge carriers in the CBM+1 state.

CONCLUSIONS

In summary, we highlight the unique advantage of detuning states coupling to prolong the hot carrier lifetime without the restriction of excitation densities employed by other methods for hot carrier solar cells, such as those based on the hot phonon bottleneck effect. The relaxation rate is proportional to the strength of the coupling between two states. ^{39,40} Simple incorporation of polar MA cations into the lattice introduces dynamic disorder which localizes charge densities and decouples the carriers in the CBM+1 and CBM states leading to an unexpected slow carrier cooling from CBM+1 to CBM. Noteworthy, this slow cooling process is independent of excitation density, which makes the perovskite hot carrier solar cell possible under one sun illumination. In addition, a slow hot carrier cooling process has been observed in the perovskite nanocrystal systems caused by increasing separation of energy states with decreasing nanocrystal size.⁷ Although the buildup time of the ground-state bleaching at the

band edge has slowed down to ~ 15 ps with the optimal nanocrystal size, the corresponding component in this work is still about 7 times longer which further highlights the promise of the hot carrier photovoltaics. We also show a list of the related works about hot carrier relaxation time and excitation density (supplemental information Table S5). There are two ways to evaluate the hot carrier relaxation time. One is to directly measure the rising time of the photobleaching peak. Compared to these results, we observe a much slower rising component about 98 ps. The other way is an indirect method to extract carrier temperature by fitting hot carrier distribution. Our slow-rising component is still 1.6 times higher than the slowest result without the limitation of excitation density.

To evaluate the improvement of the PCE with this slow hot carrier cooling, an ideal hot carrier solar cell is designed based on the utilization of the IS. Firstly, we calculate the theory maximum PCE which is about 30.7% with the bandgap of 1.59 eV (Figure S7 and Note S5). Then, it is assumed that all excited carriers with energy above the IS will relax through the IS and the carriers at IS can be perfectly extracted with appropriate electron and hole transport layers. With these assumptions, the hot carrier solar cell can be regarded as a tandem solar cell with the bandgap energies of 1.59 eV and 2.35 eV in one material. Therefore, the theoretical PCE can be elevated from 30.7% to 36.2% which promotes the S-Q limit about 20% (Figure. S7 and Note S5). Our calculation is based on the observation of the IS in this work (2.35 eV above VBM). If the energy gap of the split-off states can be tuned, this theoretical S-Q limit can be further boosted. Moreover, to evaluate the effects of hot carriers on PCE, we fabricate devices with the structure of ITO/SnO₂/perovskite/spiro-OMeTAD/Au and measure J-V characteristics (Figure S8). With the characteristics of hot carriers having excess energy, it can

be predicted that the hot carrier solar cell should have larger open-circuit voltage ($V_{\rm OC}$). Although the operational hot carrier solar cells have not been realized presently, some studies show that the prolonged hot carrier relaxation process can increase the $V_{\rm OC}$ due to the efficient extraction of hot electrons. Even though the bandgap of MACl-14 is smaller than that of MACl-0, it shows that the device based on MACl-14 has a higher $V_{\rm OC}$ (1.18 V) compared to that of MACl-0 (0.96 V), which possibly results from the prolonged hot carrier relaxation. This further demonstrates that there should be more hot carriers relax through the intermediate state in MACl-14.

EXPERIMENTAL PROCEDURES

Resource availability

Lead contact

Ti Wang serves as the lead contact (wangti@whu.edu.cn).

Materials availability

No new reagents were generated in this study.

Data and code availability

All data are available upon reasonable request.

Methods

Thin film preparation. PbI₂ solution (1.3 M, dissolved in DMF: DMSO (95: 5, v: v)) was spun cast onto the ITO substrate at 1500 rpm for 30 s and annealed at 70 °C for 1 min in nitrogen-filled glovebox. Then, the mixed organic amine salt solutions consisting of FAI (60 mg/mL) and MACl (6-14 mg/mL) (dissolved in isopropanol) were spun cast onto the PbI₂ film at 1500 rpm for 30 s and annealed in ambient air (35 RH %) at 145 °C for 13 min.

Ultrafast transient absorption. The output of a femtosecond laser (repetition rate of 40 kHz, 1030 nm central wavelength, and pulse duration of ~ 120 fs, PHAROS, Light Conversion) was split into two parts. One went through optical parametric amplification (ORPHEUS twins, Light Conversion) and then became a pump to excite perovskite thin films. The other went through the delay stage and produced white light via sapphire acting as the probe light. The pump and probe were focused on the sample with a spot size of about 64 μ m. Owing to the small angle between the two beams, the pump was blocked by the pinhole. The probe was therefore collected with a spectrometer. The above configurations were carried out with an ultrafast transient absorption spectrometer (HARPIA, Light Conversion).

Ab initio calculation. The DFT calculations are performed using VASP. $^{41-43}$ The Perdew–Burke–Ernzerhof (PBE) exchange-correlation functional is used. 44 We use $4 \times 4 \times 4$ k-point mesh to sample the Brozillon zone in geometry optimization, and static calculations using PBE functional, while $2 \times 2 \times 2$ is used to perform MD and static calculations using HSE06 functional. The simulation cell is modeled by a $2 \times 2 \times 2$ unit cell of the cubic phase of FAPbI₃. The band structure is calculated with spin-orbit coupling and PBE functional, while the DOS is calculated with spin-orbit coupling and HSE06 functional

ACKNOWLEDGMENTS

The authors acknowledge the support from the Ministry of Science and Technology of China (grant no. 2019YFE0120300), the National Natural Science Foundation of China (NSFC, Grant No. 11904266 and 91850207), the Fundamental Research Funds for the Central Universities (No. 2042021kf0202), and the Open Project Program of Wuhan National Laboratory for Optoelectronics No. 2020WNLOKF014.

AUTHOR CONTRIBUTIONS

C.W. and T.W. designed the experiments. C.W., Z.O., Z.L., and Q.G. carried out the measurements, and W.C. and O.P. carried out the calculation. F.Y. and G.F. designed and provided the materials to study. C.W. and T.W. wrote the manuscript. All authors edited the manuscript.

DECLARATION OF INTERESTS

The authors declare no competing financial interest.

REFERENCES

- 1. Shockley, W., and Queisser, H.J. (1961). Detailed balance limit of efficiency of p-n junction solar cells. J. Appl. Phys. *32*, 510-519.
- 2. Kojima, A., Teshima, K., Shirai, Y., and Miyasaka, T. (2009). Organometal halide perovskites as visible-light sensitizers for photovoltaic cells. J. Am. Chem. Soc. *131*, 6050-6051.

- 3. Jeong, J., Kim, M., Seo, J., Lu, H., Ahlawat, P., Mishra, A., Yang, Y., Hope, M.A., Eickemeyer, F.T., and Kim, M. (2021). Pseudo-halide anion engineering for α-FAPbI₃ perovskite solar cells. Nature *592*, 381-385.
- 4. Yoo, J.J., Seo, G., Chua, M.R., Park, T.G., Lu, Y., Rotermund, F., Kim, Y.-K., Moon, C.S., Jeon, N.J., and Correa-Baena, J.-P. (2021). Efficient perovskite solar cells via improved carrier management. Nature *590*, 587-593.
- 5. Min, H., Kim, M., Lee, S.-U., Kim, H., Kim, G., Choi, K., Lee, J.H., and Seok, S.I. (2019). Efficient, stable solar cells by using inherent bandgap of α-phase formamidinium lead iodide. Science *366*, 749-753.
- 6. NREL https://www.nrel.gov/pv/cell-efficiency.html.
- 7. Dai, L., Deng, Z., Auras, F., Goodwin, H., Zhang, Z., Walmsley, J.C., Bristowe, P.D., Deschler, F., and Greenham, N.C. (2021). Slow carrier relaxation in tin-based perovskite nanocrystals. Nat. Photonics *15*, 696-702.
- 8. Li, M., Fu, J., Xu, Q., and Sum, T.C. (2019). Slow hot-carrier cooling in halide perovskites: Prospects for hot-carrier solar cells. Adv. Mater. *31*, 1802486.
- 9. Zhu, H., Miyata, K., Fu, Y., Wang, J., Joshi, P.P., Niesner, D., Williams, K.W., Jin, S., and Zhu, X.-Y. (2016). Screening in crystalline liquids protects energetic carriers in hybrid perovskites. Science *353*, 1409-1413.
- 10. Yang, J., Wen, X., Xia, H., Sheng, R., Ma, Q., Kim, J., Tapping, P., Harada, T., Kee, T.W., and Huang, F. (2017). Acoustic-optical phonon up-conversion and hot-phonon bottleneck in lead-halide perovskites. Nat. Commun. *8*, 1-9.
- 11. Nie, Z., Gao, X., Ren, Y., Xia, S., Wang, Y., Shi, Y., Zhao, J., and Wang, Y. (2020). Harnessing hot phonon bottleneck in metal halide perovskite nanocrystals via interfacial electron–phonon coupling. Nano Lett. *20*, 4610-4617.
- 12. Wang, T., Jin, L., Hidalgo, J., Chu, W., Snaider, J.M., Deng, S., Zhu, T., Lai, B., Prezhdo, O., and Correa-Baena, J.-P. (2020). Protecting hot carriers by tuning hybrid perovskite structures with alkali cations. Sci. Adv. 6, eabb1336.
- 13. Price, M.B., Butkus, J., Jellicoe, T.C., Sadhanala, A., Briane, A., Halpert, J.E., Broch, K., Hodgkiss, J.M., Friend, R.H., and Deschler, F. (2015). Hot-carrier cooling and photoinduced refractive index changes in organic–inorganic lead halide perovskites. Nat. Commun. *6*, 8420. 10.1038/ncomms9420.
- 14. Li, M., Bhaumik, S., Goh, T.W., Kumar, M.S., Yantara, N., Grätzel, M., Mhaisalkar, S., Mathews, N., and Sum, T.C. (2017). Slow cooling and highly efficient extraction of hot carriers in colloidal perovskite nanocrystals. Nat. Commun. 8, 1-10.
- 15. Yang, Y., Ostrowski, D.P., France, R.M., Zhu, K., Van De Lagemaat, J., Luther, J.M., and Beard, M.C. (2016). Observation of a hot-phonon bottleneck in lead-iodide perovskites. Nat. Photonics *10*, 53-59.
- 16. Monahan, D.M., Guo, L., Lin, J., Dou, L., Yang, P., and Fleming, G.R. (2017). Room-temperature coherent optical phonon in 2D electronic spectra of CH₃NH₃PbI₃ perovskite as a possible cooling bottleneck. J. Phys. Chem. Lett. *8*, 3211-3215.
- 17. Fu, J., Xu, Q., Han, G., Wu, B., Huan, C.H.A., Leek, M.L., and Sum, T.C. (2017). Hot carrier cooling mechanisms in halide perovskites. Nat. Commun. *8*, 1-9.

- 18. Conibeer, G., Ekins-Daukes, N., Guillemoles, J.-F., Kőnig, D., Cho, E.-C., Jiang, C.-W., Shrestha, S., and Green, M. (2009). Progress on hot carrier cells. Sol. Energy Mater. Sol. Cells *93*, 713-719.
- 19. Xue, J., Wang, R., Chen, X., Yao, C., Jin, X., Wang, K.-L., Huang, W., Huang, T., Zhao, Y., and Zhai, Y. (2021). Reconfiguring the band-edge states of photovoltaic perovskites by conjugated organic cations. Science *371*, 636-640.
- 20. Yin, W.-J., Yang, J.-H., Kang, J., Yan, Y., and Wei, S.-H. (2015). Halide perovskite materials for solar cells: a theoretical review. J. Mater. Chem. A *3*, 8926-8942.
- 21. Manser, J.S., Christians, J.A., and Kamat, P.V. (2016). Intriguing optoelectronic properties of metal halide perovskites. Chem. Rev. *116*, 12956-13008.
- 22. Chen, J., Messing, M.E., Zheng, K., and Pullerits, T. (2019). Cation-dependent hot carrier cooling in halide perovskite nanocrystals. J. Am. Chem. Soc. *141*, 3532-3540.
- 23. Even, J., Pedesseau, L., Jancu, J.-M., and Katan, C. (2013). Importance of spin—orbit coupling in hybrid organic/inorganic perovskites for photovoltaic applications. J. Phys. Chem. Lett. *4*, 2999-3005.
- 24. Wei, Z., Guo, D., Thieme, J., Katan, C., Caselli, V.M., Even, J., and Savenije, T.J. (2019). The importance of relativistic effects on two-photon absorption spectra in metal halide perovskites. Nat. Commun. *10*, 1-8.
- 25. Even, J., Pedesseau, L., Dupertuis, M.-A., Jancu, J.-M., and Katan, C. (2012). Electronic model for self-assembled hybrid organic/perovskite semiconductors: Reverse band edge electronic states ordering and spin-orbit coupling. Phys. Rev. B 86, 205301.
- Ye, F., Ma, J., Chen, C., Wang, H., Xu, Y., Zhang, S., Wang, T., Tao, C., and Fang, G. (2021). Roles of MACl in sequentially deposited bromine-free perovskite absorbers for efficient solar cells. Adv. Mater. 33, 2007126.
- 27. Yang, G., Zhang, H., Li, G., and Fang, G. (2019). Stabilizer-assisted growth of formamdinium-based perovskites for highly efficient and stable planar solar cells with over 22% efficiency. Nano Energy *63*, 103835.
- 28. Manser, J.S., and Kamat, P.V. (2014). Band filling with free charge carriers in organometal halide perovskites. Nat. Photonics *8*, 737-743.
- 29. Guo, Z., Wan, Y., Yang, M., Snaider, J., Zhu, K., and Huang, L. (2017). Long-range hot-carrier transport in hybrid perovskites visualized by ultrafast microscopy. Science *356*, 59-62.
- 30. Qing, J., Liu, X.K., Li, M., Liu, F., Yuan, Z., Tiukalova, E., Yan, Z., Duchamp, M., Chen, S., and Wang, Y. (2018). Aligned and graded type-II Ruddlesden–Popper perovskite films for efficient solar cells. Adv. Energy Mater. *8*, 1800185.
- 31. Kim, M., Kim, G.-H., Lee, T.K., Choi, I.W., Choi, H.W., Jo, Y., Yoon, Y.J., Kim, J.W., Lee, J., and Huh, D. (2019). Methylammonium chloride induces intermediate phase stabilization for efficient perovskite solar cells. Joule *3*, 2179-2192.
- 32. Mateen, M., Arain, Z., Yang, Y., Liu, X., Ma, S., Liu, C., Ding, Y., Ding, X., Cai, M., and Dai, S. (2020). MACl-induced intermediate engineering for high-performance mixed-cation perovskite solar cells. ACS Appl. Mat. Interfaces *12*, 10535-10543.

- 33. Chen, K., Barker, A.J., Morgan, F.L., Halpert, J.E., and Hodgkiss, J.M. (2015). Effect of carrier thermalization dynamics on light emission and amplification in organometal halide perovskites. J. Phys. Chem. Lett. *6*, 153-158.
- 34. Xing, G., Mathews, N., Sun, S., Lim, S.S., Lam, Y.M., Grätzel, M., Mhaisalkar, S., and Sum, T.C. (2013). Long-range balanced electron-and hole-transport lengths in organic-inorganic CH₃NH₃PbI₃. Science *342*, 344-347.
- 35. Yang, Z., Surrente, A., Galkowski, K., Bruyant, N., Maude, D.K., Haghighirad, A.A., Snaith, H.J., Plochocka, P., and Nicholas, R.J. (2017). Unraveling the exciton binding energy and the dielectric constant in single-crystal methylammonium lead triiodide perovskite. J. Phys. Chem. Lett. *8*, 1851-1855.
- 36. Katan, C., Pedesseau, L., Kepenekian, M., Rolland, A., and Even, J. (2015). Interplay of spin—orbit coupling and lattice distortion in metal substituted 3D tri-chloride hybrid perovskites. J. Mater. Chem. A *3*, 9232-9240.
- 37. Yaffe, O., Guo, Y., Tan, L.Z., Egger, D.A., Hull, T., Stoumpos, C.C., Zheng, F., Heinz, T.F., Kronik, L., and Kanatzidis, M.G. (2017). Local polar fluctuations in lead halide perovskite crystals. Phys. Rev. Lett. *118*, 136001.
- 38. Li, W., Vasenko, A.S., Tang, J., and Prezhdo, O.V. (2019). Anharmonicity extends carrier lifetimes in lead halide perovskites at elevated temperatures. J. Phys. Chem. Lett. *10*, 6219-6226.
- 39. Nieto-Pescador, J., Abraham, B., and Gundlach, L. (2014). Photoinduced ultrafast heterogeneous electron transfer at molecule–semiconductor interfaces. J. Phys. Chem. Lett. *5*, 3498-3507.
- 40. Wang, T., Liu, Q., Caraiani, C., Zhang, Y., Wu, J., and Chan, W.-L. (2015). Effect of interlayer coupling on ultrafast charge transfer from semiconducting molecules to mono-and bilayer graphene. Phys. Rev. Applied *4*, 014016.
- 41. Kresse, G., and Hafner, J. (1993). Ab initio molecular dynamics for liquid metals. Phys. Rev. B *47*, 558.
- 42. Kresse, G., and Furthmüller, J. (1996). Efficiency of ab-initio total energy calculations for metals and semiconductors using a plane-wave basis set. Comput. Mater. Sci. 6, 15-50.
- 43. Kresse, G., and Furthmüller, J. (1996). Efficient iterative schemes for ab initio total-energy calculations using a plane-wave basis set. Phys. Rev. B *54*, 11169.
- 44. Kresse, G., and Joubert, D. (1999). From ultrasoft pseudopotentials to the projector augmented-wave method. Phys. Rev. B *59*, 1758.

FIGURES

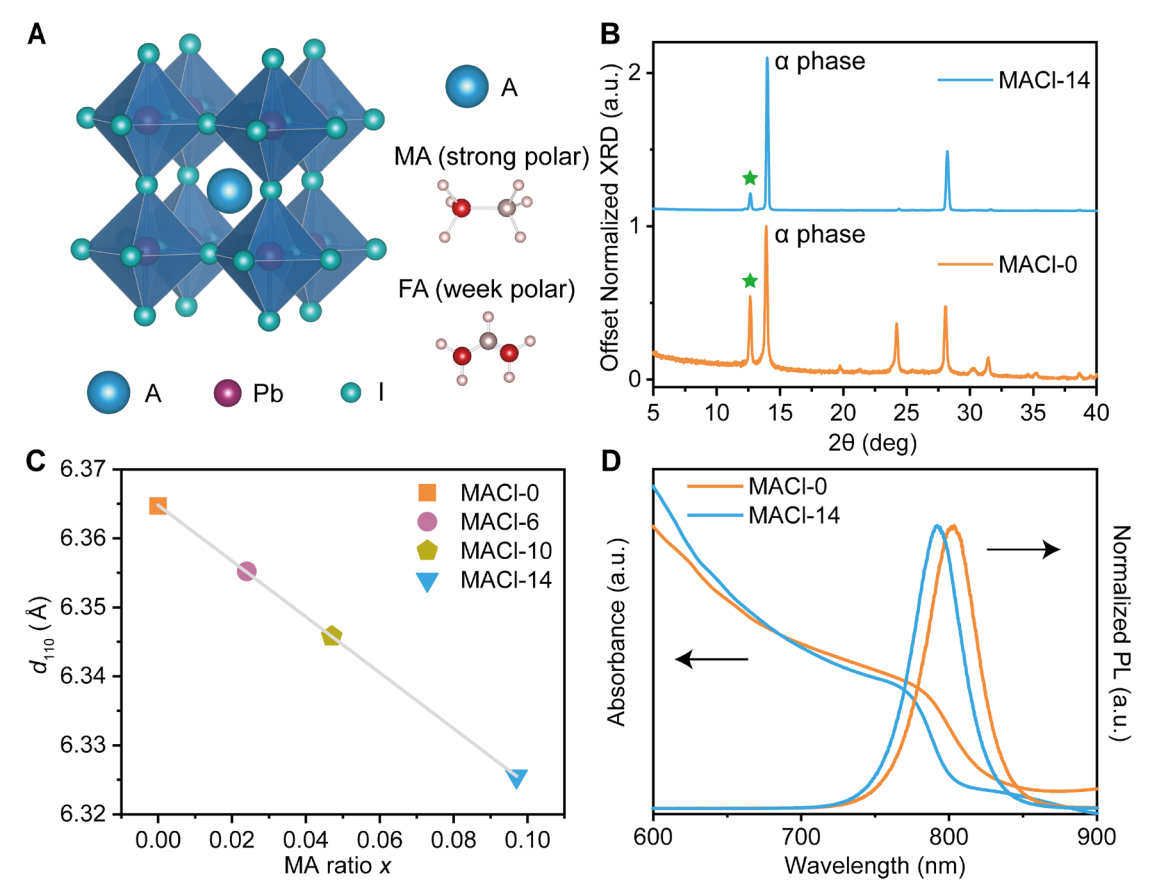


Figure 1. Crystal structures and optical properties of FAPbI₃ with the MA cation incorporation.

- (A) The crystal structure of hybrid perovskites APbI₃. The A-site organic cation can be MA or FA.
- (B) XRD patterns of MACl-0 and MACl-14. The peaks at $\sim 14^{\circ}$ represent the (110) plane of the α phase, and the peaks marked with a green star are related to PbI₂.
- (C) The spacing of (110) plane d_{110} are extracted from XRD (110) peak positions. The solid line is a linear fitting of the d_{110} .
- (D) Absorption and PL spectra of MACl-0, MACl-14, respectively.

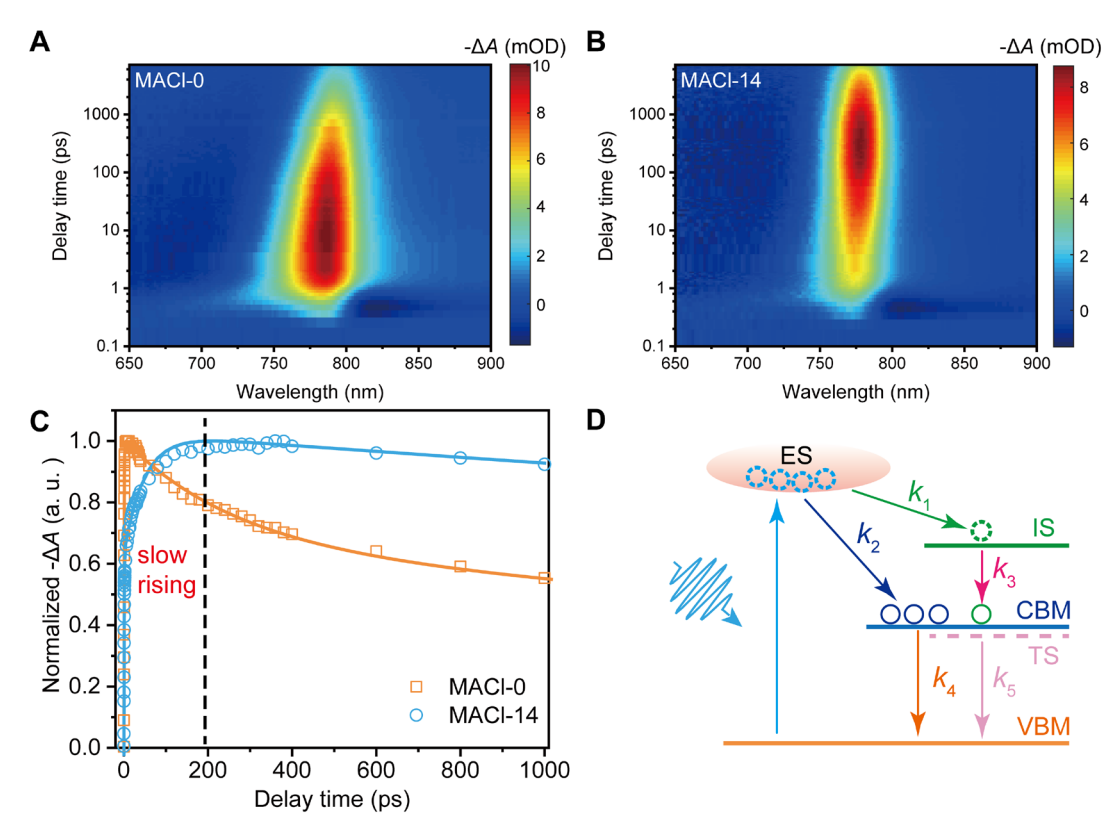


Figure 2. Slow-rising component of carrier dynamics.

- (A-B) Pseudo TA color images of MACl-0 and MACl-14 with an excitation photon energy of 3.10 eV.
- (C) Normalized bleaching dynamics for MACl-0 and MACl-14. The solid lines are the fitting results.
- (D) Schematic drawing of the carrier relaxation process with a three-level energy system model. ES: excited states; IS: intermediate states; CBM: conduction band minimum; VBM: valance band maximum; TS: trap states.

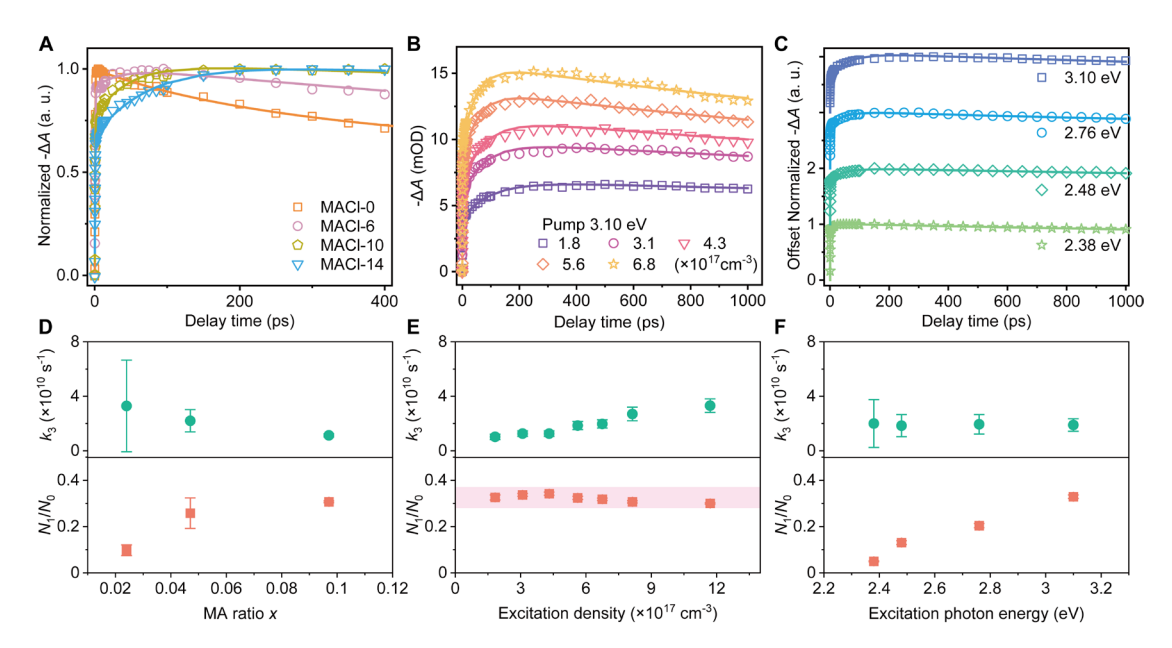


Figure 3. Hot carrier cooling with the influence of MA cations, excitation densities and excitation photon energy.

- (A) Normalized bleaching dynamics of different samples with the excitation photon energy of 3.10 eV. The pump fluence keeps the same for different photon energies. The slow-rising component becomes obvious with increasing MA ratio.
- (B) Normalized bleaching dynamics of MACl-14 under various excitation densities. The excitation photon energy is 3.10 eV. The slow-rising component changes slightly with the excitation energy.
- (C) Normalized bleaching dynamics under different excitation photon energies of the MACl-14 sample. The pump fluence is unchanged. The slow-rising component fades away with the decrease of the excitation energy.
- (D-F) The fitting parameters of (A-C) with our three-level energy system model, respectively. The k_3 is the relaxation rate from IS to CBM and the parameter N_1/N_0 depicts the portion of carrier relaxation through IS. It presents that k_3 rate is impacted by the MA ratio. The parameter N_1/N_0 is independent of excitation density and the IS is about 2.35 eV above the VBM.

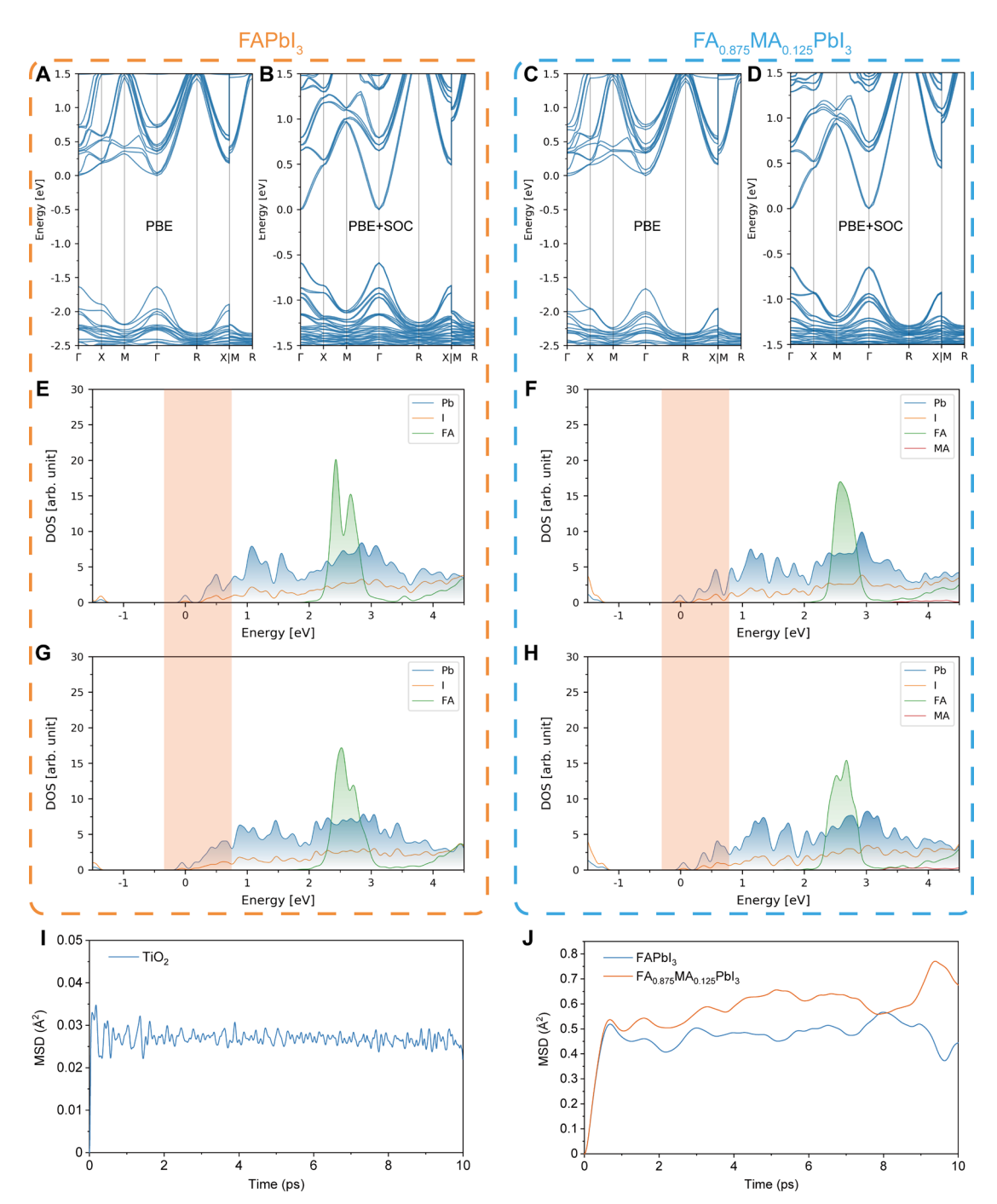


Figure 4. The SOC and electron-phonon coupling in hybrid perovskites.

- (A-D) The band structure of FAPbI₃ and FA_{0.875}MA_{0.125}PbI₃ calculated with/without SOC. A large split-off of CBM and CBM+1 exists when the SOC is considered.
- (E-H) Density of states of two representative snapshots of FAPbI₃ and FA $_{0.875}$ MA $_{0.125}$ PbI₃. Both HSE06 functional and the SOC are employed. The electronic structure near CBM fluctuates more in FAPbI₃ than FA $_{0.875}$ MA $_{0.125}$ PbI₃, the gap from the first two isolated peaks often disappears in FAPbI₃.
- (I and J) Mean square displacement of the inorganic lattice of FAPbI₃/FA_{0.875}MA_{0.125}PbI₃, and a representative conventional semiconductor TiO₂ in a 10 ps molecular dynamics simulation.